collimations 10′-20′-20′-20′ we obtained a wavevector resolution of $\delta Q/Q = 0.0020$.

Inelastic neutron scattering. A 50-g powder sample was sealed with ^{4}He exchange gas in a thin-walled aluminium can for the inelastic neutron-scattering experiments at the NIST centre for neutron research. For energy transfers <40 meV we used a direct geometry time-of-flight (TOF) spectrometer in the neutron energy gain mode with a PG(002) double crystal monochromator set at $E_i = 3.55$ meV and a cooled beryllium filter in the incident beam. The elastic energy resolution was 0.2 meV. Low temperature (10 K) neutron energy gain data served as a direct measure of the background. For energy transfer from 40 to 200 meV we used a filter analyser (FA) spectrometer with a Cu(220) monochromator surrounded by 60′-40′ horizontal collimation and combined with a cooled polycrystalline beryllium filter as the analyser. The relative energy resolution of this instrument was ~8% in the energy range probed. The fast neutron background in the FA experiment was measured and subtracted. We also subtracted a constant background arising from the finite transmission through the FA of elastically scattered thermal neutrons. The scale factor between the TOF and FA data was determined by comparing the integrated intensity associated with the 37-meV peak in the phonon spectrum of ZrW_2O_8 (Fig. 1). Absolute normalization of the TOF data was accomplished by measuring the count rate associated with incoherent elastic scattering from a known amount of vanadium.

Analysis of neutron scattering data. In the limit of large wavevector transfer, Q, the one-phonon double differential scattering cross-section can be approximated[9,10] by:

$$\frac{d^2\sigma}{d\Omega dE'} = \frac{k'}{k}\left(N\sum_{i=1}^{n}\frac{(\hbar Q)^2}{2M_i}b_i^2\, e^{-2W_i(Q)}Z_i(\omega)\right)\frac{n(\omega)+1}{\hbar\omega} \quad (1)$$

Here the sum is over all atoms in one unit cell, k and k' are the initial and final neutron wavevectors, respectively, b_i is bound coherent neutron scattering length, M_i is the atomic mass, $Z_i(\omega)$ is the contribution of atom i to the phonon density of states and $n(\omega) = (\exp(\hbar\omega/k_BT) - 1)^{-1}$ is the Bose population factor. The Debye–Waller factor, $\exp(-2W_i(Q))$, is related to the mean-square atomic displacements given by Evans *et al.*[11] The quantity which can be extracted from inelastic neutron scattering is the so-called generalized phonon density of states $g(\omega)$ defined by:

$$g(\omega) = \sum_{i=1}^{n}\frac{b_i^2}{2M_i}e^{-2W_i(Q)}Z_i(\omega)\Bigg/\sum_{i=1}^{n}\frac{b_i^2}{2M_i}e^{-2W_i(Q)} \quad (2)$$

Concerning the relationship between $g(\omega)$ and $Z(\omega)$ we note that for ZrW_2O_8, the neutron scattering lengths of the different atoms are very similar, and the differences in the atomic masses are partially compensated by the Debye–Waller factors. Nevertheless, we expect that vibrations of the lighter oxygen atoms are weighted more heavily in $g(\omega)$ than in the true state density, $Z(\omega)$.

Received 27 May; accepted 11 August 1998.

1. Martinek, C. & Hummel, F. A. Linear thermal expansion of three tungstates. *J. Am. Ceram. Soc.* **51,** 227–228 (1968).
2. Mary, T. A., Evans, J. S. O., Vogt, T. & Sleight, A. W. Negative thermal expansion from 0.3 to 1050 Kelvin in ZrW_2O_8. *Science* **272,** 90–92 (1996).
3. Fleming, D. A., Johnson, D. W. & Lemaire, P. J. US Patent No. 5694503 (1997).
4. Blackman, M. On the thermal expansion of solids. *Proc. Phys. Soc. B* **70,** 827–832 (1957).
5. Giddy, A. P., Dove, M. T., Pawley, G. S. & Heine, V. The determination of rigid unit modes as potential soft modes for displacive phase transitions in framework crystal structures. *Acta Crystallogr. A* **49,** 697–703 (1993).
6. Pryde, A. K. A. *et al.* Origin of the negative thermal expansion in ZrW_2O_8 and ZrV_2O_7. *J. Phys. Condens. Matter* **8,** 10973–10982 (1996).
7. Barron, T. H. K., Collins, J. G. & White, G. K. Thermal expansion of solids at low temperatures. *Adv. Phys.* **29,** 609–730 (1980).
8. Ramirez, A. P. & Kowach, G. R. Large low temperature specific heat in the negative thermal expansion compound ZrW_2O_8. *Phys. Rev. Lett.* **80,** 4903–4906 (1998).
9. Lovesey, S. W. *Theory of Neutron Scattering from Condensed Matter* Vol. 1 (Clarendon, Oxford, 1984).
10. Squires, G. L. *Introduction to the Theory of Thermal Neutron Scattering* (Cambridge Univ. Press, 1978).
11. Evans, J. S. O., Mary, T. A., Vogt, T., Subramanian, M. A. & Sleight, A. W. Negative thermal expansion in ZrW_2O_8 and HfW_2O_8. *Chem. Mater.* **8,** 2809–2823 (1996).

Acknowledgements. We thank W. Kamitakahara, P. Littlewood, D. Neuman, A. Pinczuk, T. Siegrist, C. Varma, T. Yildrim and in particular S. Simon for discussions. Work at JHU was supported by the NSF; this work used neutron research facilities supported by NIST and the NSF.

Correspondence and requests for materials should be addressed to A.P.R. (e-mail: apr@bell-labs.com).

Five parametric resonances in a microelectromechanical system

Kimberly L. Turner*, Scott A. Miller†‡, Peter G. Hartwell§, Noel C. MacDonald§, Steven H. Strogatz* & Scott G. Adams*†

** Department of Theoretical and Applied Mechanics, † School of Applied and Engineering Physics, § School of Electrical Engineering and the Cornell Nanofabrication Facility, Cornell University, Ithaca, New York 14853-5401, USA*
‡ Present address: Kionix, Inc., 22 Thornwood Drive, Ithaca, New York 14850, USA.

The Mathieu equation[1] governs the forced motion of a swing[2], the stability of ships[3] and columns[4], Faraday surface wave patterns on water[5,6], the dynamics of electrons in Penning traps[7], and the behaviour of parametric amplifiers based on electronic[8] or superconducting devices[9]. Theory predicts that parametric resonances occur near drive frequencies of $2\omega_0/n$, where ω_0 is the system's natural frequency and n is an integer ≥ 1. But in macroscopic systems, only the first instability region can typically be observed, because of damping and the exponential narrowing[10] of the regions with increasing n. Here we report parametrically excited torsional oscillations in a single-crystal silicon microelectromechanical system. Five instability regions can be measured, due to the low damping, stability and precise frequency control achievable in this system. The centre frequencies of the instability regions agree with theoretical predictions. We propose an application that uses parametric excitation to reduce the parasitic signal in capacitive sensing with microelectromechanical systems. Our results suggest that microelectromechanical systems can provide a unique testing ground for dynamical phenomena that are difficult to detect in macroscopic systems.

The micromachining field has been given the generic name microelectromechanical systems. This field is quite broad, and

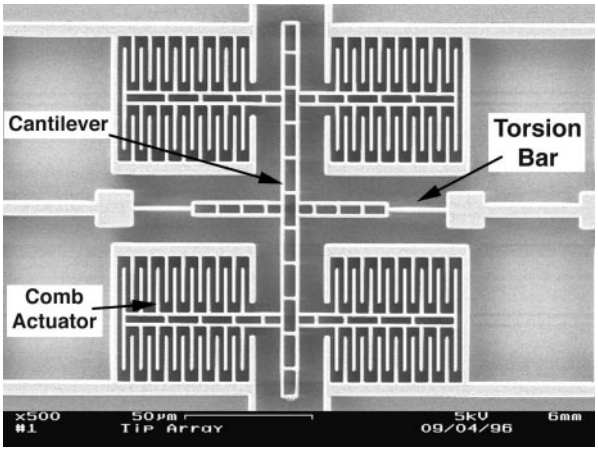

Figure 1 Scanning electron microscope image of the torsional oscillator. This oscillator is the out-of-plane motion actuator for arrays of scanning tunnelling microscopes[12]. A typical device covers an area of ~150 μm^2. The relevant parameters for this device are: $k \approx 2.75 \times 10^{-8}$ N m, $I = 2.12 \times 10^{-19}$ kg m^2, $\gamma = 1.216 \times 10^{-12}$ N m V^{-2} and $Q \approx 3000$ (see text for definition of symbols). The maximum signal amplitude applied to the device was 38 V. The device is fabricated using conventional integrated-circuit technology from single-crystal silicon.

includes integrated microsensors, microactuators, microinstruments[11], micro-optics and microfluidics. Applications include accelerometers to deploy an air bag in a car; ink-jet printer heads; an array of movable mirrors for colour projection displays; and atom probes for imaging and transporting atoms[12,13]. Microinstrumentation for micrometre/nanometre scale fluidics[14], when coupled with microanalytical instrumentation, offers possibilities in characterizing mechanical and rheological properties of biological molecules. Microelectromechanical systems typically use silicon as a structural material, and the devices are fabricated using conventional integrated-circuit technology.

The devices we consider here are microelectromechanical probes used for scanned-probe microscopy, including scanning tunnelling microscopy and atomic force microscopy. They are fabricated from single-crystal silicon. As shown in Fig. 1, the device consists of a cantilevered beam connected to a torsion bar. Attached to the cantilevered beam are an atomically sharp tip for the probe and comb capacitive transducers for sensing and actuation. The same capacitive transducer design, which is the source of the parametric excitation in this system, can be used either for sensing displacements or for inducing motion. As an actuator, the interdigitated capacitive plates used here allow for a wide range of motion and reasonably high amplitudes without failure. This type of actuator generates out-of-plane motion forces due to a phenomenon known as comb-drive levitation[15]. In this technique, a voltage is applied to the fixed electrodes, while the silicon substrate and movable electrodes are grounded. This causes asymmetrical fringing electric fields between the movable and fixed electrodes, and these fields induce motion in the movable electrodes, one of which is illustrated in a cross-sectional view in Fig. 2a.

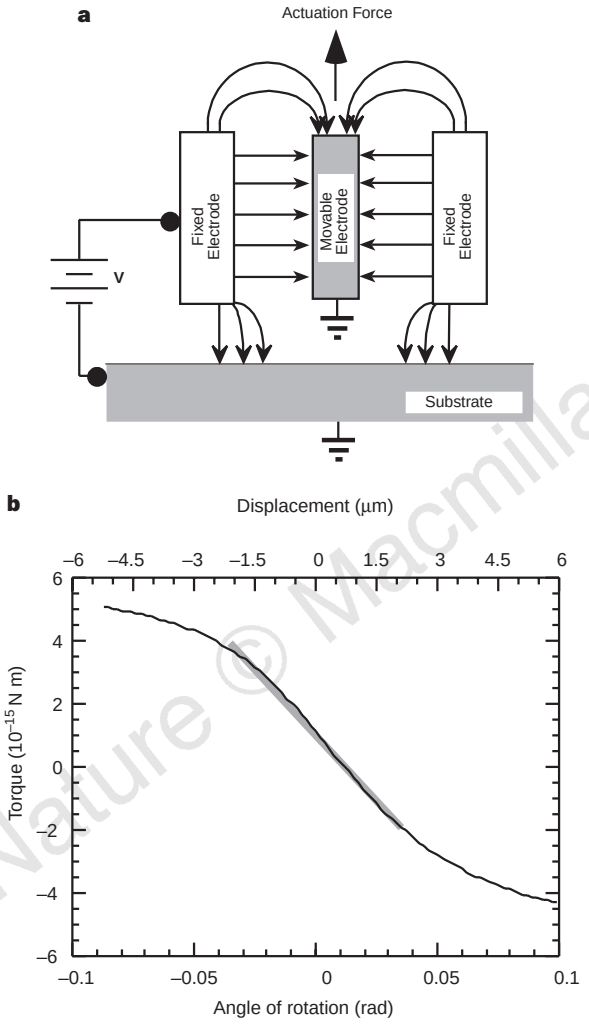

Figure 2 Comb-drive levitation of torsional oscillator. **a**, Schematic of comb-drive levitation with one movable electrode and two fixed electrodes. The actual device has a total of 16 movable electrodes on each side. In modelling, we assumed that the metal-coated interdigitated fingers were perfect conductors. The beams were modelled as 1 μm wide, 20 μm long and 10 μm deep, with a 2 μm gap between electrodes and a distance of 5 μm between the device electrodes and the substrate. The simplified model consisted of one movable electrode between two fixed ones. The results were then generalized to include all 32 actuation electrodes in the particular device being studied. **b**, Torsional simulation results: torque generated versus angle of rotation for one movable electrode and two fixed electrodes. Displacement of the end of the cantilever is also displayed on the top axis. During device operation, the maximum rotation obtained is 0.017 rad. This shows that for the region of operation we are concerned with, the torque generated versus angle rotated curve can be approximated as linear ($R = 0.997$). The region of possible operation on this curve is highlighted, to show that the linear approximation is suitable in this case.

To estimate the out-of-plane forces and torques generated by the comb-drive levitation effect, we have performed a three-dimensional electrostatic simulation using COULOMB[16], an electrostatic boundary element method solver. A graph of the computed electrostatic torque versus angle of rotation for one movable electrode is shown in Fig. 2b.

The operational mode of the device is an out-of-plane torsional vibration. Although the system is continuous, much of its behaviour can be understood by a simplified one-degree-of-freedom model that treats the torsional mode separately. The equation of motion is:

$$I\ddot{\theta} + c\dot{\theta} + k\theta = M(t,\theta) \qquad (1)$$

where θ is the rotation angle of the torsion bar (the overdot denotes differentiation with respect to time), I is the mass moment of inertia of the torsional cantilever, c is the torsional damping constant, k is the torsional stiffness, and M is the applied torque. As a first approximation, we assume that the damping and restoring forces are linear. For the torsional members used here, made of single-crystal silicon, the quality factor Q has been measured to be ~3,000 at 18 mtorr. The torque is $M(t,\theta) = V^2\phi(\theta)$, where V is the applied voltage and $\phi(\theta)$ gives the angular dependence of the torque generated by comb-drive levitation. Applying a voltage $V = (A_{DC} + A_{AC}\cos\omega t)^{1/2}$ yields $M(t,\theta) = (A_{DC} + A_{AC}\cos\omega t)\phi(\theta)$, where A_{DC} and A_{AC} are the magnitudes of the direct current and alternating current of the input signal, respectively. From results of the simulations shown in Fig. 2b, $\phi(\theta)$ can be approximated as linear

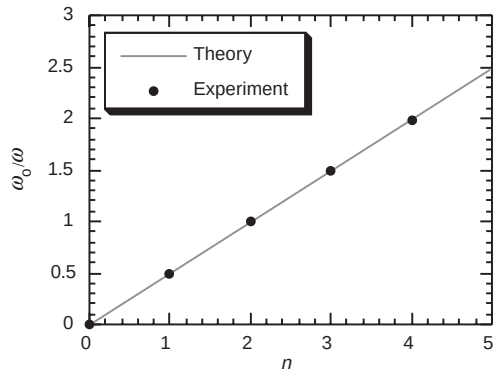

Figure 3 Theoretical prediction and experimental measurements of the frequency ratio for the centre of the nth parametric resonance region. Results for five regions are shown. The instability frequencies match theoretical values to within 0.7%. Reasons for error between predicted values and actual instabilities include errors in the calculated device parameters, errors in the force simulation (geometrical assumptions) and in the ability to accurately locate the 'centre' of the instability region, as the regions tend to be asymmetric due to damping effects.

if we assume small-angle rotations: $\phi(\theta) = -\gamma\theta$. In actual operation, the device rotates a maximum of 0.017 rad, making the small-angle approximation appropriate. Using this approximation and defining $\tau = \omega t$, the equation of motion becomes:

$$\theta'' + \frac{c}{\omega I}\theta' + \frac{1}{\omega^2 I}(k + \gamma A_{DC} + \gamma A_{AC}\cos\tau)\theta = 0 \qquad (2)$$

where prime denotes differentiation with respect to τ.

Equation (2) is a damped Mathieu equation of the form

$$\theta'' + a\theta' + (b + d\cos\tau)\theta = 0 \qquad (3)$$

where $a = c/\omega I$, $b = (k + \gamma A_{DC})/\omega^2 I$, and $d = \gamma A_{AC}/\omega^2 I$. The theory developed for the Mathieu equation allows us to predict the frequencies where parametric resonances will occur. Assuming weak periodic forcing and negligible damping, first-order perturbation theory predicts instabilities centred at $b = n^2/4$, for $n = 1, 2, \ldots$. This result implies that parametric resonance occurs at drive frequencies $\omega = 2\omega_0/n$, where ω_0 denotes the natural frequency of the torsional mode.

To test these predictions experimentally, we used an unusual technique in which a laser vibrometer is mounted on an optical microscope. The laser beam is sent through the microscope and focused on the movable microelectromechanical device. This enables nanometre-scale displacements of the device to be accurately resolved. After a preliminary estimate of the frequency of the first Mathieu instability, given by $\omega = 2\omega_0 = 2\sqrt{k/I}$, an experimental frequency sweep was used to establish ω_0 more precisely. Then the formula $\omega = 2\omega_0/n$ predicted the drive frequencies where the other Mathieu instabilities should be centred.

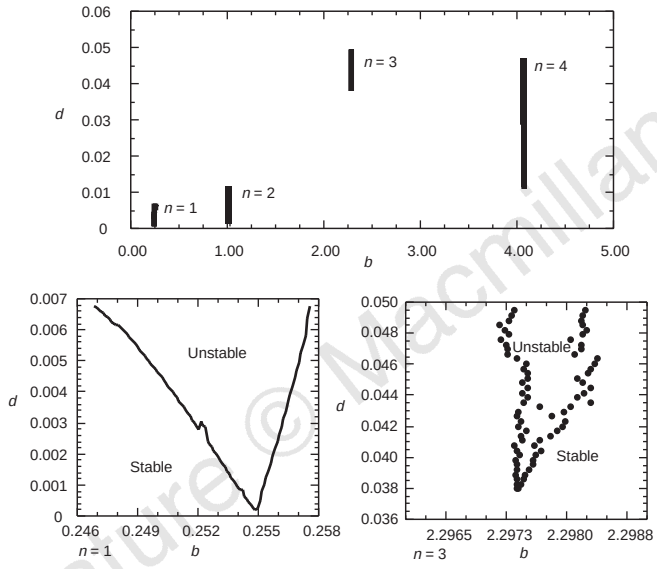

Figure 4 Instability map for $n = 1$–4. The top panel shows a general view of this map. When studying parametric resonance in such systems, it is useful to consider only those instabilities that correspond to odd n. When using comb-drive levitation for actuation, there is a small asymmetry in the torque versus angle function (see Fig. 2b). This asymmetry directly adds an additional driving term to the right-hand side of equation (1). For driving frequencies which are not integer multiples of the natural frequency of the device, the term will not affect the Mathieu response of the system. However, when the natural frequency is an integer multiple of the drive frequency (that is, $n = 2$, 4) the driving term on the right-hand side will have fundamental and/or harmonic components which are at the natural frequency of the device, therefore driving it into resonance and coupling with any parametric resonance also present. As the first and third regions can be directly compared to theory, experimental plots of these regions are magnified to show more detail (bottom two panels). Of considerable interest is the linear shape of the $n = 1$ boundary as predicted from theory. The bottom of the curve rounds off due to damping. The boundaries for the third instability region are not linear. This is also predicted from theory[1]. Differences between the mathematical prediction of the shape and the actual shape of the region are primarily due to imperfect stability of the testing set-up. Localized laser heating, drift of the laser spot on the device, room conditions, and variable conditions in the vacuum chamber also contribute to small shifts in the instability boundaries. For higher-order stability maps ($n \geq 3$), the tests can take up to 36 hours to run. Stability over time becomes an issue, as small changes in the system cause the instability boundary to shift.

Five Mathieu instabilities predicted by equation (3) were experimentally observed. Figure 3 plots the frequency ratio ω_0/ω for the observed Mathieu instabilities, along with the theoretical prediction $\omega_0/\omega = n/2$. The agreement is within 0.7% at all points.

The theory of the Mathieu equation shows that each resonance occurs within a 'tongue' in the (b, d) parameter space for equation (3). The shape and position of the tongues are affected by damping of the system. Damping has the stabilizing effect of 'raising' the tongue higher up in the parameter space, as well as narrowing the unstable regions. Because of the extreme narrowness of high-order tongues, they are hard to resolve and are rarely observed in macroscopic systems. In our system, several Mathieu tongues could be mapped experimentally, due to the device's low damping, the precise and stable frequency control on the drive, and the sensitivity of the laser vibrometer technique. Figure 4 is a plot of the instability regions for $n = 1$–4, including magnified views of the tongues for $n = 1$ and $n = 3$. Upper limits in d for each instability are not absolute; they are merely where each experiment was stopped in order to limit the voltage amplitude to the device. The measured boundaries between stability and instability are linear for $n = 1$, which is predicted for the damped Mathieu equation.

The parametric resonances reported here suggest a way to reduce the parasitic signals in capacitive sensing with microelectromechanical systems. The motion of many such systems can be detected as changes in the capacitance between movable and fixed elements. Unfortunately, parasitic signals can be a problem; because the devices are small, and the electrical isolation is not perfect, there is some coupling of the actuating drive signal to the sensing capacitors. This stray signal can easily overshadow any change in capacitance due to the motion of the system in question.

The idea is to separate the drive and sense signals by parametrically exciting the device far from its natural frequency. This is only possible in systems governed by Mathieu-type equations, due to the unique way energy is transferred during parametric excitation. For example, we consider a given device with a natural frequency of $\omega_0 = 57$ kHz driven at the frequency ω corresponding to the first Mathieu instability ($n = 1$); here $\omega = 2\omega_0/n = 114$ kHz. The parasitic signal from the incoming drive will also be at 114 kHz. However, the device will still vibrate torsionally at its natural frequency of 57 kHz, so the capacitive sensing signals of interest will also be at 57 kHz. With this separation in frequency, it is straightforward to filter out the parasitic 114-kHz signal, thereby revealing the 57-kHz sensing signal.

Additionally, when operated in the first instability region, the device can be used to increase sensitivity in atomic force microscopy (AFM) measurements. In conventional AFM, high Q leads to higher sensitivity, at the expense of bandwidth. By utilizing the parametric resonance instability, the effect of Q can be decoupled from sensitivity. At the edge of the instability region, the device has a 0.001 Hz in 114 kHz turn-on (that is, a shift of 10 parts per billion will move the response from stable to unstable). This is a much sharper transition than obtainable with high-Q cantilevers used in present resonance mode AFM techniques. □

Received 16 March; accepted 11 August 1998.

1. Grimshaw, R. *Nonlinear Ordinary Differential Equations* 62–79 (Blackwell, Oxford, 1990).
2. Burns, J. A. More on pumping a swing. *Am. J. Phys.* **38,** 920–922 (1970).
3. Ruby, L. Applications of the Mathieu equation. *Am. J. Phys.* **64,** 39–44 (1996).
4. Nayfeh, A. H. & Mook, D. T. *Nonlinear Oscillations* (Wiley, New York, 1979).
5. Faraday, M. On the forms and states assumed by fluids in contact with vibrating elastic surfaces. *Phil. Trans. R. Soc. Lond.* **121,** 319–340 (1831).

6. Rayleigh, Lord *The Theory of Sound* Vol. II 346–350 (Dover, New York, 1944).
7. Tan, J. & Gabrielse, G. Synchronization of parametrically pumped electron oscillators with phase bistability. *Phys. Rev. Lett.* **67,** 3090–3093 (1991).
8. Howson, D. P. & Smith, R. B. *Parametric Amplifiers* (McGraw-Hill, New York, 1970).
9. Likharev, K. K. *Dynamics of Josephson Junctions and Circuits* (Gordon & Breach Science, Philadelphia, 1986).
10. Levy, D. M. & Keller, J. B. Instability intervals of Hill's equation. *Commun. Pure Appl. Math.* **16,** 458–476 (1963).
11. Saif, M. T. A. & MacDonald, N. C. Measurement of forces and spring constants of microinstruments. *Rev. Sci. Instrum.* **69,** 1410–1422 (1998).
12. Miller, S. A., Turner, K. L. & MacDonald, N. C. Microelectromechanical scanning probe instruments for array architectures. *Rev. Sci. Instrum.* **68,** 4155–4162 (1997).
13. Timp, G. (ed.) *Nano-Science and Technology* (AIP, Woodbury, in the press).
14. Carr, W. N. (ed.) *J. Micromech. Microeng.* **4,** (4: special issue on microfluids) (1994).
15. Tang, W. C., Lim, M. G. & Howe, R. T. Electrostatic comb drive levitation and control method. *J. MicroElectroMechan. Syst.* **1,** 170–178 (1992).
16. COULOMB (Integrated Engineering Software, Inc., 1989).

Acknowledgements. We thank F. Bertsch for experimental assistance. This work was supported in part by the National Science Foundation and the Defense Advanced Research Projects Agency.

Correspondence and requests for materials should be addressed to K.L.T. (e-mail: turner@tam.cornell.edu).

Generalized syntheses of large-pore mesoporous metal oxides with semicrystalline frameworks

Peidong Yang*, Dongyuan Zhao*†, David I. Margolese*, Bradley F. Chmelka†‡ & Galen D. Stucky*†

* *Departments of Chemistry and Materials,* † *Materials Research Laboratory,* ‡ *Department of Chemical Engineering, University of California, Santa Barbara, California 93106, USA*

Surfactants have been shown to organize silica into a variety of mesoporous forms, through the mediation of electrostatic, hydrogen-bonding, covalent and van der Waals interactions[1–8]. This approach to mesostructured materials has been extended, with sporadic success, to non-silica oxides[5–17], which might promise applications involving electron transfer or magnetic interactions. Here we report a simple and versatile procedure for the synthesis of thermally stable, ordered, large-pore (up to 140 Å) mesoporous metal oxides, including TiO_2, ZrO_2, Al_2O_3, Nb_2O_5, Ta_2O_5, WO_3, HfO_2, SnO_2, and mixed oxides $SiAlO_{3.5}$, $SiTiO_4$, $ZrTiO_4$, Al_2TiO_5 and ZrW_2O_8. We used amphiphilic poly(alkylene oxide) block copolymers as structure-directing agents in non-aqueous solutions for organizing the network-forming metal-oxide species, for which inorganic salts serve as precursors. Whereas the pore walls of surfactant-templated mesoporous silica[1] are amorphous, our mesoporous oxides contain nanocrystalline domains within relatively thick amorphous walls. We believe that these materials are formed through a mechanism that combines block copolymer self-assembly with complexation of the inorganic species.

In a typical synthesis, 1 g of poly(alkylene oxide) block copolymer $HO(CH_2CH_2O)_{20}(CH_2CH(CH_3)O)_{70}(CH_2CH_2O)_{20}H$ (designated $EO_{20}PO_{70}EO_{20}$; Pluronic P-123, BASF) was dissolved in 10 g of ethanol (EtOH). To this solution, 0.01 mol of the respective inorganic chloride precursor (Table 1) was added with vigorous stirring for 1/2 h. The resulting sol solution was gelled in an open Petri dish at 40 °C in air for 1–7 days, during which the inorganic precursor hydrolyses and polymerizes into a metal oxide network. Alternatively, the sol solution can be used to prepare thin films by dip coating. All as-made samples are transparent except for the samples derived from WO_3, which are dark blue. The as-made bulk samples or thin films were then calcined at 400 °C for 5 h in air to remove the surfactant species. Figure 1a shows typical X-ray diffraction (XRD) patterns for mesostructured zirconium oxides before and after calcination. The as-made zirconium inorganic/polymer mesostructure shows three diffraction peaks with lattice spacings $d = 115$, 65 and 59 Å. After calcination, the diffraction peaks appear at higher 2θ angles with $d = 106$, 60 and 53 Å. Both sets of diffraction peaks can be indexed as the (100), (110) and (200) reflections from two-dimensional hexagonal mesostructures with lattice constants $a = 132$ and 122 Å, respectively.

When $HO(CH_2CH_2O)_{106}(CH_2CH(CH_3)O)_{70}(CH_2CH_2O)_{106}H$ (abbreviated as $EO_{106}PO_{70}EO_{106}$) and $HO(CH_2CH_2O)_{75}(CH_2CH(CH_3CH_2)O)_{45}H$ (that is, $EO_{75}BO_{45}$) are used as the structure-directing agents under the above conditions, cubic mesophases are formed. Figure 1b shows the XRD patterns for the mesostructured TiO_2 formed using $EO_{75}BO_{45}$. The low-angle XRD pattern for the as-made samples shows six resolved peaks with d spacings of 100, 70, 58, 44, 41 and 25 Å. These peaks display d-value ratios of $\sqrt{2} : \sqrt{4} : \sqrt{6} : \sqrt{10} : \sqrt{12} : \sqrt{32}$, which are indexable as (110), (200), (211), (310), (222) and (440) reflections respectively, in the cubic $Im\bar{3}m$ space group. Following calcination of the sample at 400 °C, three XRD peaks are observed with d spacings of 76, 53 and 43 Å (ratios $\sqrt{2} : \sqrt{4} : \sqrt{6}$), which are similarly indexable as (110), (200) and (211) reflections of the cubic $Im\bar{3}m$ mesophase.

This synthetic procedure has been successfully applied to the preparation of mesoporous TiO_2, ZrO_2, Al_2O_3, Nb_2O_5, WO_3, HfO_2, SnO_2, and mixed oxides $SiAlO_{3.5}$, $SiTiO_4$, $ZrTiO_4$, Al_2TiO_5, ZrW_2O_8. Table 1 summarizes the d_{100} values measured for these different calcined oxides, along with other physical characteristics and material properties. All calcined samples show ordering lengths that are greater than 70 Å.

The appearance of low-angle diffraction peaks indicates that mesoscopic order is preserved in the calcined metal oxide materials. This is confirmed by transmission electron microscopy (TEM) images obtained from each of these samples. For example, Fig. 2a–f shows TEM images of mesoporous TiO_2, ZrO_2, Nb_2O_5 and $SiAlO_{3.5}$ recorded along the [110] and [001] zone axes of the mesostructures. In each case, well-ordered large channels are clearly observed to be arranged in hexagonal arrays. The pore/channel walls are continuous and have thicknesses of ~40–70 Å (Table 1). In addition, energy dispersive X-ray spectroscopy (EDX) measurements and quantitative elemental analysis made on each of the calcined samples show the expected primary metal element signals, along with very weak Cl signals, which confirm that the inorganic walls consist of predominantly metal–oxygen networks. Local EDX

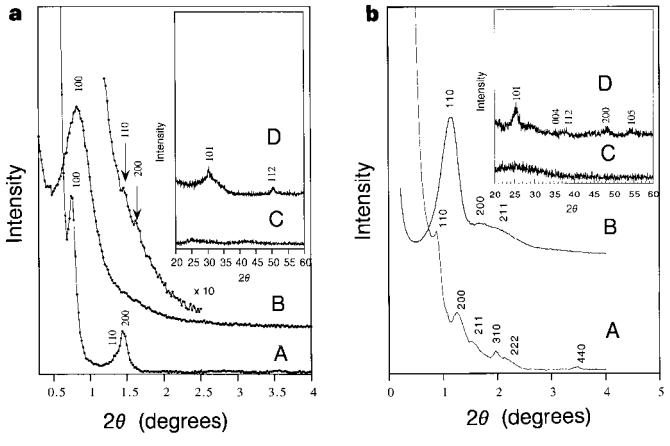

Figure 1 Powder X-ray diffraction patterns for mesoporous ZrO_2 (**a**) and TiO_2 (**b**). Traces A and C are low-angle and wide-angle XRD patterns of the as-made inorganic/$EO_{20}PO_{70}EO_{20}$ composite mesostructures, which have amorphous frameworks. Traces B and D are low-angle and wide-angle XRD patterns for the same mesoporous oxides calcined at 400 °C for 5 h in air. The high-angle diffractions are indexed according to their corresponding crystalline oxide phases. The XRD patterns were obtained with a Scintag PADX diffractometer using Cu Kα radiation.